On the collision between deep anticyclones and seamounts

Gordon E. Swaters

Applied Mathematics Institute, Department of Mathematical Sciences, and Institute for Geophysical Research, University of Alberta, Edmonton, T6G 2G1, Canada

Abstract – Numerical simulations of the collision between deep topographically-steered anticyclonic eddies and seamounts are described. The simulations are based on a two-layer intermediate length-scale model which filters out barotropic processes and focuses on the sub-inertial baroclinic dynamics within the context of allowing finite-amplitude height variations in the deep cold eddies and a background topographic vorticity gradient. © 2001 Éditions scientifiques et médicales Elsevier SAS

anticyclonic eddies / sub-inertial baroclinic dynamics

1. Introduction and model description

The dynamics of deep density-driven currents and eddies plays an important role in the redistribution of oceanic water masses. Examples include, for example, the equatorward flow of bottom intensified boundary currents such as the Denmark Strait overflow or the propagation of Antarctic Bottom Water. In general, the currents associated with these moving water masses correspond to geostrophically balanced density driven flows on a sloping bottom. Numerical simulations and theory have revealed that these currents can exhibit vigorous baroclinic instability which can saturate as bottom intensified along slope propagating anticyclones (Swaters [1]) which remain relatively coherent for hundreds of days.

In this paper we examine numerically the propagation characteristics of these deep eddies when they encounter an orographic anomaly in their path. There many anomalies one can choose to examine such as ridges, troughs or canyons. We will look at what happens when a deep anticyclone interacts with a seamount. Even within this class of topographic anomalies, one can look at direct hits, glancing interactions, multiple seamounts, radially and non-radially symmetric obstacles and so on. The list is endless.

Here, we examine only one class of deep eddy-seamount interactions in a series of three numerical simulations. We shall look at the direct head-on collision between an initially isolated steadily propagating deep anticyclone and a radially symmetric seamount which is twice the diameter of the anticyclone. The three simulations correspond to a seamount with a height which is small, on the same scale and tall, respectively, compared to the scale height of the anticyclone. Roughly speaking, as we shall see, the collision between a deep anticyclone results, not surprisingly, in a spatial distortion in the eddy and the excitation of topographic Rossby waves in the surrounding water. The Rossby waves act to radiate energy away from the propagating anticyclone which results in the down slope motion of the eddy even after the eddy has propagated past the seamount. Since the background sloping topography acts like a topographic β-plane in the dynamics of the surrounding fluid, one can think of the induced down slope motion as a 'southward' deflection.

E-mail address: gordon.swaters@ualberta.ca (G.E. Swaters).

Indeed, we believe that our results are relevant to the development of a general understanding of the dynamics of density-driven vortices in a stratified ocean which propagate on a background vorticity gradient such as, for example, westward propagating eddies on a β-plane, which collide with a seamount. An example might include zonally propagating 'meddies' which interact with seamounts in the Atlantic Ocean (Richardson et al. [2]).

The model we use to examine the collision between a deep anticyclone or cold dome and a seamount is the two-layer model of Swaters and Flierl [3] and Swaters [4]. This model is based on a sub-inertial approximation to the shallow water equations in which the geostrophic pressure in the upper layer (see *figure 1*) is principally driven by baroclinic vortex-tube stretching and a background topographic vorticity gradient. The lower layer, i.e., the eddy layer, while geostrophic, allows for finite-amplitude thickness variations in order to allow for eddies in the lower layer which possess a genuine incropping (i.e., the location where the lower layer height intersects the bottom, that is, an 'abyssal outcropping'). The mean flow in the lower layer arises primarily due to a geostrophic balance between the Coriolis stress and the down slope gravitational acceleration associated with a relatively dense water mass sitting directly on a sloping bottom. This model filters out barotropic instabilities in the eddy layer and focuses on the baroclinic dynamics of density-driven currents and eddies on a sloping bottom.

The stability characteristics seen in more sophisticated 3D numerical simulations for density-driven flows on a sloping bottom (e.g., Jiang and Garwood [5,6]; Chapman and Gawarkiewicz [7] and Gawarkiewicz and Chapman [8]) are well described by the present model (Swaters [1]) as are laboratory experiments on the formation of deep anticyclones from density-driven flows (e.g., Lane-Serff and Baines [9]; Choboter and Swaters [10]).

The plan of the paper is as follows. In the remainder of this section we briefly describe the model. In section 2 we describe the propagating isolated cold dome solutions to the model. These will be the initial condition we use in our simulations. In section 3 we describe our simulations and in section 4 we summarize our results.

1.1. Model formulation

Since the derivation of the equations has been describe elsewhere (e.g., Swaters and Flierl [3]; Swaters [4]), our presentation will be brief. The physical geometry corresponds to a two-layer fluid (see *figure 1*) on a f-plane with x and y the along-shore and offshore coordinates, respectively, and t is time. Alphabetical subscripts, except where indicated, represent partial differentiation.

If the geostrophic pressure or stream function in the upper layer is denoted by $\eta(x, y, t)$ and the lower layer current height, relative to the height of the variable bottom topography denoted by $h_B(x, y)$, is denoted as $h(x, y, t)$, then the non-dimensional model can be written in the form

$$\Delta \eta_t + J(h + \eta, h_B) + J(\eta, \Delta \eta) = 0, \tag{1}$$
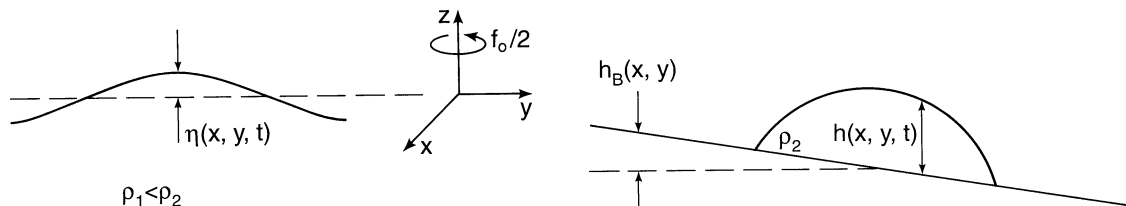
$$h_t + J(\eta + h_B, h) = 0, \tag{2}$$

Figure 1. Geometry of the model used in this paper.

where $J(A, B) \equiv A_x B_y - A_y B_x$. Given η and h, the velocity in the upper and lower layers and the geostrophic pressure in the lower layer are given by, respectively,

$$\mathbf{u}_1 = \hat{e}_3 \times \nabla \eta, \tag{3}$$

$$\mathbf{u}_2 = \hat{e}_3 \times \nabla(\eta + h + h_B), \tag{4}$$

$$p = h_B + \eta + h. \tag{5}$$

The non-dimensional variables are related to the dimensional (asterisked) variables via the relations

$$
\begin{aligned}
(x^*, y^*) &= L(x, y), & t^* &= (sf)^{-1}t, & h^* &= sHh, \\
\mathbf{u}_1^* &= sfL\mathbf{u}_1, & \eta^* &= s(fL)^2 g^{-1}\eta, & \mathbf{u}_2^* &= sg'H(fL)^{-1}\mathbf{u}_2, \\
h_B^* &= sHh_B, & p^* &= s\rho_2 g'Hp,
\end{aligned}
\tag{6}
$$

where the horizontal length scale is the internal deformation radius $L = \sqrt{g'H}/f$ associated with the upper layer, g' is the reduced gravity and

$$s = \frac{s^*L}{H} = \frac{s^*g'/f_0}{\sqrt{g'H}}, \tag{7}$$

is a scaled bottom slope parameter where s^* is the unscaled bottom slope parameter and H is the mean depth of the upper layer.

Equations (1) and (2) correspond to an asymptotic limit (i.e., $0 < s \ll 1$) of the full two-layer shallow water equations in which the evolution of the upper layer is quasi-geostrophic but the lower layer, while geostrophic, is not quasi-geostrophic and allows for large-amplitude thickness variations, i.e., allows for cold dome or eddy configurations in which the lower layer height can intersect the bottom.

Nof [11] showed that, for a fully nonlinear reduced gravity shallow water model, all isolated steadily travelling eddies on a constant sloping bottom travel in the along slope direction with speed s^*g'/f_0 which we call the 'Nof speed'. The parameter s is the ratio of the Nof speed to the speed of long or irrotational internal gravity waves in a reduced gravity model.

The dimensional values associated with the above scalings depend on the local environmental parameters. For example, for the cold pool described by Houghton et al. [12], the time scale is about 7 days, the horizontal length scale is about 12 km and the lower layer velocity scale is about 2.5 cm/s (Swaters [4]).

From the point of view of interpreting the model in the context of potential vorticity dynamics, we note that $1 + 2$ is the O(s) potential vorticity equation associated with the upper layer. Equation (2) is the O(1) potential vorticity equation associated with the lower layer. Since the lower layer dynamics does not include inertia, we may interpret the lower layer model as a planetary geostrophic balance (see, e.g., Pedlosky [13]) scaled appropriately for shelf dynamics in which the background vorticity gradient is provided by the sloping bottom. Unlike many planetary geostrophic models (e.g., de Verdiere [14]), (1) and (2) does not exhibit an ultra-violet catastrophe in the instability problem.

We note that the two-layer model described here has been extended to allow for a continuously-stratified upper layer (Poulin and Swaters [15–17]). The reason we numerically integrate the two-layer model here is that we are presently only just developing the numerical code for the continuously-stratified model and it was unavailable for these simulations. A meta-theory of two-layer models of the sort used in this paper can be found in Karsten and Swaters [18].

2. Deep anticyclonic vortices

Mory et al. [19] describe rotating-tank experiments on bottom-trapped domes. These experiments (and others, e.g., Whitehead et al. [20]) clearly indicate that there was an appreciable azimuthal velocity field formed above the eddy in the surrounding eddy which was at least as large as the swirl velocity (i.e. the azimuthal velocity in the co-moving frame) in the eddy itself.

The importance of the upper layer can be seen in the 'Stern Isolation Constraint' (Mory [21]) which, for (1) and (2), can be expressed in the form

$$\iint_{\mathbb{R}^2} h + \eta \, \mathrm{d}x \, \mathrm{d}y = 0 \tag{8}$$

(Swaters and Flierl [3]). This constraint, which in our context is equivalent to a zero topographic Rossby wave condition in the upper layer, must be satisfied by 'all' isolated steadily-travelling solutions to (1) and (2) or its full two-layer analogue (Mory [21]). Since $h \geqslant 0$ everywhere, the Stern isolation constraint clearly suggests that there must be a region of cyclonic circulation over top of the travelling dome and this is what is observed in the rotating tank experiments.

Nevertheless, Swaters and Flierl [3] found a class of exact steadily-travelling isolated eddy solutions to (1) and (2) for constant sloping topography which travel with the Nof velocity. These solutions are the baroclinic analogues of the equivalent-barotropic or reduced gravity solutions found by Nof [11].

Assuming $h_B = -y$ and a radially-symmetric eddy of the form

$$h(r) = \begin{cases} h_s(r), & 0 \leqslant r < a, \\ 0, & r \geqslant a, \end{cases} \tag{9}$$

assuming $h_s(a) = 0$, where a is the eddy radius and where r is the radial coordinate in the co-moving frame, i.e.,

$$r \equiv \sqrt{(x - t - x_0)^2 + (y - y_0)^2},$$

where (x_0, y_0) is arbitrary, then η, which is the solution of

$$\Delta \eta + \eta = -h,$$

subject to the radiation condition

$$\lim_{r \to \infty} r^{1/2} \eta = 0 \quad \text{in the sector } \left| \tan^{-1}\left(\frac{y}{x}\right) \right| < \frac{\pi}{2},$$

is given by

$$\eta(r) = \begin{cases} \eta_s(r), & 0 \leqslant r < a, \\ 0, & r \geqslant a, \end{cases} \tag{10}$$

where

$$\eta_s(r) = -\frac{\pi Y_0(r)}{2} \int_0^r \xi J_0(\xi) h_s(\xi) \, \mathrm{d}\xi - \frac{\pi J_0(r)}{2} \int_r^a \xi Y_0(\xi) h_s(\xi) \, \mathrm{d}\xi, \tag{11}$$

with the zero topographic Rossby wave condition

$$\int_0^a \xi J_0(\xi) h_s(\xi) \, \mathrm{d}\xi = 0. \tag{12}$$

These baroclinic solutions travel with the Nof velocity and do not exhibit any cross-slope motion. The constraint (12), which arises in order to eliminate the topographic wave field ahead of the travelling eddy in the upper layer, can shown (Swaters and Flierl [3]) to be equivalent to the Stern isolation constraint (8). It is straightforward to verify that (12) implies that $\eta_s = \eta_{s_r} = \eta_{s_{rr}} = 0$ at $r = a$.

Although there is a variational principle for these solutions, this variational principle cannot be used to examine the stability of this baroclinic eddy via an Arnol'd-like stability argument (Swaters [22]). While this failure of the Arnol'd argument to establish stability does not, of course, imply these solutions are unstable, it is nevertheless suggestive of it. However, from a phenomenological point of view, even if these solutions are dynamical unstable, they still may have an important role in ocean dynamics since the growth rates of the instabilities, if any, are long compared to the natural time scale of the eddies themselves (Swaters [1,23]).

3. Simulations

Equations (1) and (2) were numerically solved as the system

$$q_t + J(\eta, q + h_B) = 0, \tag{13}$$

$$h_t + J(\eta + h_B, h) = \nu \Delta h, \tag{14}$$

$$\Delta \eta = q - h, \tag{15}$$

where (13) is simply (1)+(2) and is the potential vorticity equation for the upper layer. Equations (13) and (14) were integrated forward in time using a 256×256 second-order leapfrog procedure with the Arakawa [24] finite difference scheme implemented for the Jacobian. A 'Robert' filter (Asselin [25]) with coefficient 0.005 was applied at each time step to suppress the computational mode. The upper layer stream function η was obtained from (15) at each time step using a direct solver. The numerical friction term Δh with coefficient $\nu = 10^{-3}$ was included in (14) to suppress high wave number features in the simulations.

The computational domain is the periodic channel

$$\Omega = \{(x, y) \mid |x| < 30, |y| < 30\}, \tag{16}$$

where the periodicity is in the x direction and we impose $\eta = 0$ on $y = \pm 30$.

We made a number of simulations before deciding on the domain size. Our goal was to have a computational domain small enough that the deep eddy or cold dome and any subsequent anomalies which might form would be adequately resolved. At the same time, the computational domain had to be large enough so that we could adequately model the development of any topographic Rossby wave field which might form. The above computational domain satisfied these requirements. Our simulations had about 58 grid points along a radial cross section within the cold dome and thus in that part of any upper layer wave field immediately over the cold dome.

The periodic boundary conditions in the x direction allows upper layer wave energy to radiate out of the domain in the along slope direction. In order to suppress wave energy from re-entering the domain along the $x = 30$ boundary, we imposed a sponge layer in the immediate neighborhood of $x = \pm 30$ with a spatially varying damping coefficient. The cross slope boundaries, i.e., $y = \pm 30$, were far enough away from the trajectory of the eddy that imposing homogeneous Dirichlet boundary conditions on η at $y = \pm 30$ did not dramatically affect our results.

The initial eddy and upper layer geostrophic pressure will be given (9) and (10), respectively, with

$$h_s(r) = \frac{1}{2}\left[1 + \cos\left(\frac{\pi r}{a}\right)\right], \tag{17}$$

where $x_0 = -18.0$ and $y_0 = 0.0$. The radius a, which is determined by (12), is about 6.85. It follows that the maximum eddy height is 1.0. The interval of time we numerically integrate the equations for is $0 \leqslant t \leqslant 35$ in each simulation.

The topography in all our simulations will be given by

$$h_B(x, y) = \begin{cases} -y + \frac{h_0}{2}\left[1 + \cos\left(\frac{\pi\sqrt{x^2+y^2}}{2a}\right)\right], & 0 \leqslant \sqrt{x^2 + y^2} < 2a, \\ -y, & \sqrt{x^2 + y^2} \geqslant 2a, \end{cases} \tag{18}$$

where h_0 is the maximum height of the seamount and a is the radius of the eddy initially. The topography corresponds to radially symmetric (continuously differentiable) seamount with radius $2a$ superimposed on a background topography which has constant slope. The background topographic slope implies that, in the absence of the seamount, the depth of the water column increases linearly as y increases, i.e. the down slope direction is in the positive y direction.

Our three simulations will have values for h_0 of 0.1, 1.0 and 5.0, respectively, which we will describe as the 'short', 'moderate height' and 'tall' seamount simulations, respectively. These values for h_0 correspond to seamount heights which are a tenth, the same and five times the maximum height of the eddy, respectively.

In *figure 2* we present a contour plot of $h_B(x, y)$ with $h_0 = 5.0$ (i.e. the 'tall' seamount). The background topography slopes downward as y increases or as one moves from the bottom to the top of the panel. Thinking in terms of a β-plane analogy, 'westward' and 'southward' correspond to increasing values of x and y, respectively, or, equivalently, moving from the left to the right and from the bottom to the top of the panel,
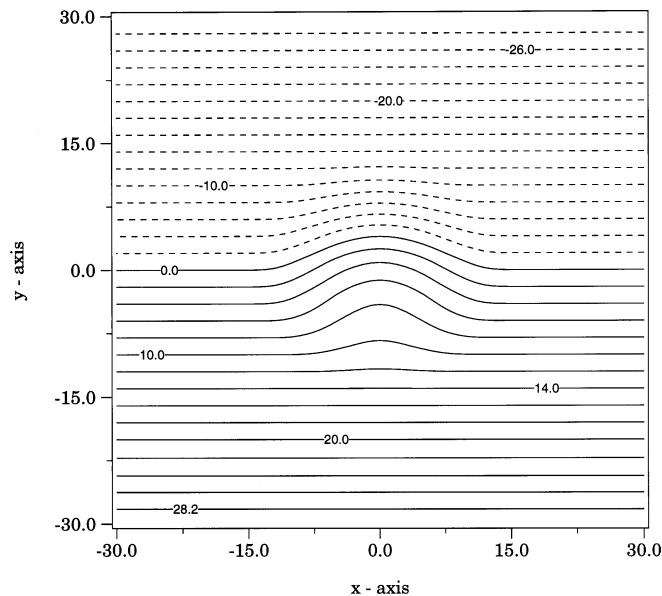

Figure 2. Contour plot of $h_B(x, y)$ for $h_0 = 5.0$. The contours correspond to lines of constant background potential vorticity in the upper layer.

respectively. The contours in *figure 2* are, in fact, isolines of constant background potential vorticity for the upper layer.

In our discussion of the numerical simulations there are some auxiliary diagnostic quantities which are useful. The first of these is the coordinates of the center of mass of the propagating eddy, denoted as $(X(t), Y(t))$, and defined by, respectively,

$$X(t) = \frac{\iint_\Omega xh(x, y, t)\, dx\, dy}{\iint_\Omega h(x, y, t)\, dx\, dy}, \tag{19}$$

$$Y(t) = \frac{\iint_\Omega yh(x, y, t)\, dx\, dy}{\iint_\Omega h(x, y, t)\, dx\, dy}. \tag{20}$$

The role of the topography and of the upper layer in determining the trajectory of the center of mass can be seen in the relations determining the velocity of the center of mass. If (19) and (20) are differentiated with respect to time, it follows that

$$\frac{dX}{dt} = -\frac{\iint_\Omega (h_{B_y} + \eta_y)h\, dx\, dy}{\iint_\Omega h\, dx\, dy}, \tag{21}$$

$$\frac{dY}{dt} = \frac{\iint_\Omega (h_{B_x} + \eta_x)h\, dx\, dy}{\iint_\Omega h\, dx\, dy}, \tag{22}$$

where we have used (2).

In the region away from the seamount, i.e., $\sqrt{x^2 + y^2} \geqslant 2a$, $h_B = -y$ and these relations reduce to

$$\frac{dX}{dt} = 1 - \frac{\iint_\Omega \eta_y h\, dx\, dy}{\iint_\Omega h\, dx\, dy}, \tag{23}$$

$$\frac{dY}{dt} = \frac{\iint_\Omega \eta_x h\, dx\, dy}{\iint_\Omega h\, dx\, dy}. \tag{24}$$

In this region we see that the center of mass of the eddy propagates with the Nof velocity, i.e., in the positive x direction with unit speed, modulated by the interaction between the eddy height field and upper layer geostrophic pressure.

If we make the additional assumption that the eddy height and upper layer geostrophic pressure are radially symmetric, as they are initially in our simulations, it follows that the integrals in the numerators in (23) and (24) are identically zero so that $(X_t, Y_t) = (1, 0)$. These are exactly the propagation characteristics associated with the Swaters and Flierl [3] baroclinic deep anticyclone solution (9) through to (12).

The potential vorticity in the upper layer is, of course, another important quantity. From (13) the upper layer potential vorticity, denoted by PV, and given by

$$PV(x, y, t) = \Delta\eta + h + h_B, \tag{25}$$

is a Lagrangian invariant.

Before turning to describing the results for each simulation it is useful to provide an outline of what we will see. The effect of the seamount on the propagating eddy and surrounding ocean will come in a sequence of stages. From (21) and (22), as the eddy approaches the seamount and the ambient topographic slope changes,

this will lead to changes in the velocity of the center of mass. This effect arises because the eddy propagates as a geostrophically balanced density driven flow on a sloping bottom, that is, it is topographically steered at least initially in the collision.

On the other hand, as the ambient depth of the upper layer changes due to the presence of the seamount, the other components in the upper layer *PV* must evolve if the *PV* is to be conserved following the motion. This evolution comes in a number of stages as well.

First, we expect that the center of mass of the eddy will attempt to follow lines of constant background potential vorticity. As the eddy encounters the seamount it will be deflected to its left or toward positive values of *y* or, in terms of the β-plane analogy, toward the 'south' (see *figure 2*).

However, the seamount does not have a constant slope associated with it. While the center of mass, which is an integrated or averaged quantity, will follow the trajectory determined by (21) and (2), individual fluid parcels within the eddy will not necessarily follow a parallel path since, from (2) which is a hyperbolic equation for h, adjacent points in the eddy height field will experience a different topographic slope induced velocity. Thus, the initial radial symmetry will be lost in the eddy height field leading to a distortion in its shape.

In such a process it is highly unlikely that the zero topographic Rossby wave condition (12) can be maintained. Hence, as the eddy begins to spatially distort as it encounters the seamount, Rossby waves will be excited in the upper layer. As shown by Swaters [23], the topographic Rossby waves act to radiate energy away from the eddy. The source of the energy is the gravitational potential energy associated with cross slope position of the eddy. That is, as the energy is being radiated away, the eddy slides down the slope toward deeper water. (This is the same sort of process as described by Flierl [26] for radiating warm eddies on a β-plane.) We should expect this down slope, or 'southward' motion thinking of the β-plane analogy, to continue even after the eddy traverses the seamount because of the continued action of the wave field in radiating energy away. In addition, as shown by Swaters [23], the dynamical feedback of the topographic Rossby wave on the eddy height field leads to the development of spiral arms on the eddy incropping further distorting the spatial shape of the eddy. All these features will be seen in the simulations which we now present.

3.1. Short seamount collision

In *figure 3* we show gray scale panels of the upper layer stream function or geostrophic pressure $\eta(x, y, t)$ (on the left) and the eddy height $h(x, y, t)$ (on the right) for $t = 0.0$, 17.5 and 35.0, respectively, for the 'short' seamount with $h_0 = 0.1$ in (18). These times correspond to the initial condition (which is the same for all the simulations), during the period in which the eddy is directly interacting with the seamount, and at the end of the simulation after the eddy has passed by the seamount, respectively. The gray scale for the upper layer geostrophic pressure panels is a straightforward linear interpolation of white (associated with the pressure maximum) through to black (associated with the pressure minimum). The gray scale for the eddy height is in comparison inverted, with white identified with zero height (i.e., no eddy) and black identified with the maximum height. The coordinate span and the orientation of each panel is identical to that in *figure 2*.

In the $t = 0.0$ panels we see the radially symmetric eddy and cyclonic upper layer pressure located at the initial point given by $(x, y) = (-18.0, 0.0)$. There is no wave field since the zero topographic Rossby wave field condition (12) holds. As the simulation proceeds, the eddy initially propagates steadily from left to right (or 'westward' in terms of the β-plane analogy) with speed 1.0 (the Nof speed) and there is no cross slope motion.

The response of the eddy to the short seamount is not dramatic. In the $t = 17.5$ panels we can see some spatial distortion developing in the eddy height field and the formation of a relatively weak crescent-shaped topographic wave tail in the upper layer geostrophic pressure field. In the $t = 35.0$ panels we see the continued
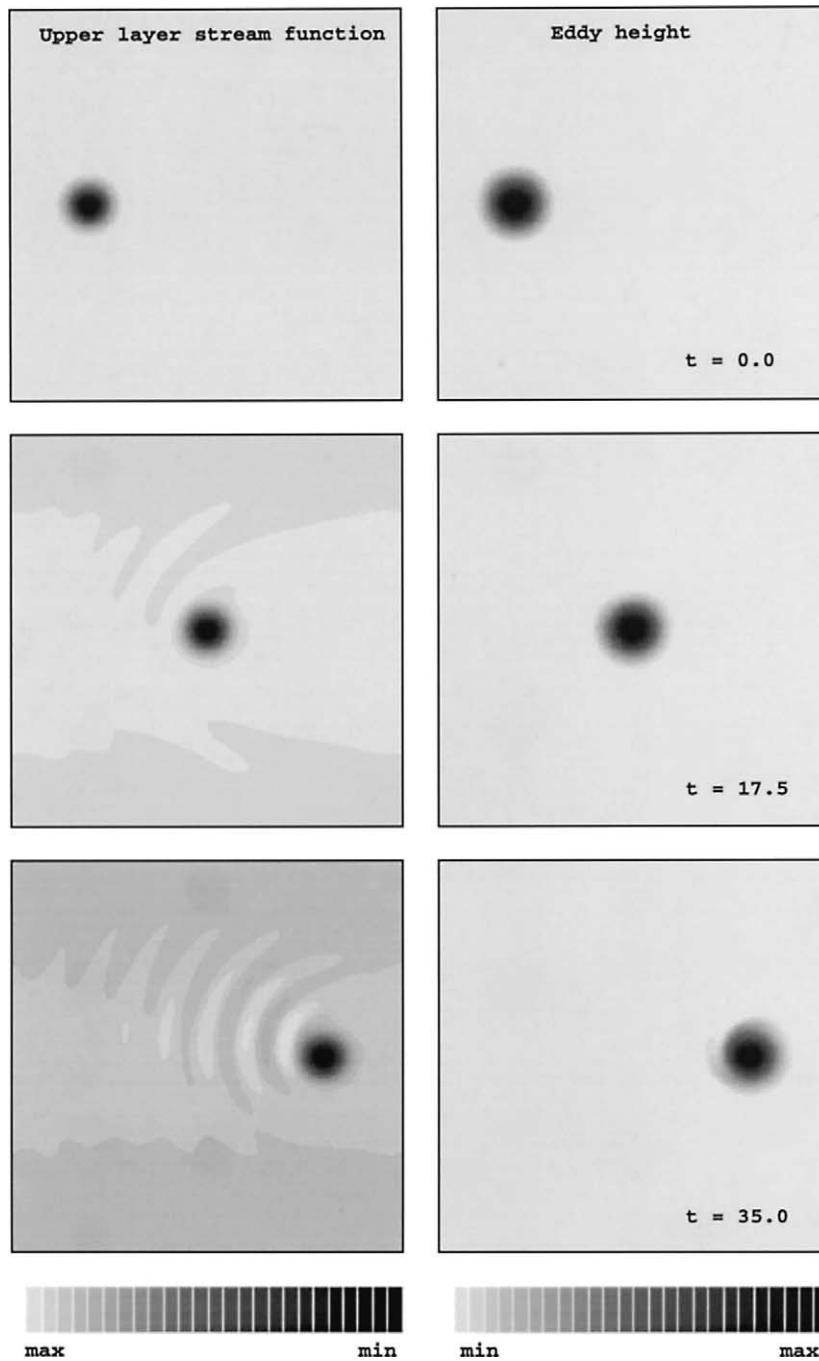
Figure 3. Gray scale panels of the upper layer stream function or geostrophic pressure $\eta(x, y, t)$ (on the left) and the eddy height $h(x, y, t)$ (on the right) for $t = 0.0$, 17.5 and 35.0, respectively, for the 'short' seamount simulation. The coordinate span and the orientation of each panel is identical to that in *figure 2*.
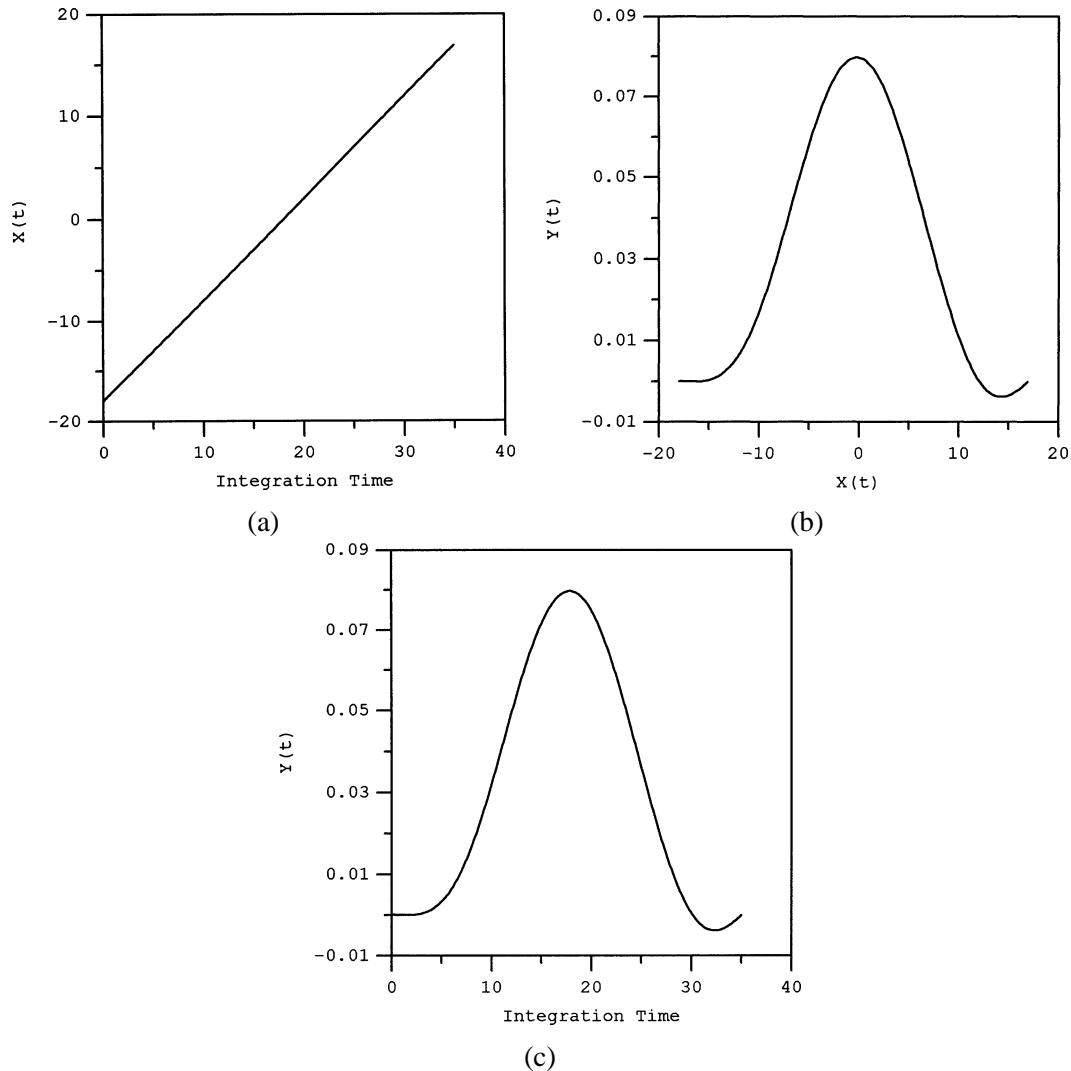
Figure 4. The center of mass coordinates (a) $X(t)$ and (b) $Y(t)$ versus the integration time, respectively, and (c) the path taken by the center of mass (X, Y), as determined by numerically evaluating (19) and (20) for the 'short' seamount simulation.

development of the relatively weak topographic Rossby wave tail and one can see the initial development of spiral arms on the boundary of the eddy height as theory predicts (Swaters [23]).

In *figures 4(a), (b)* we show the coordinates of the center of mass for this simulation versus the integration time as determined by numerically evaluating (19) and (20). One can see that throughout the entire simulation $X(t)$ develops linearly and $X_t(t) \approx 1.0$ and is well described by the Nof velocity. There is, in fact, a very slight acceleration in $X_t(t)$ as the eddy interacts directly with the seamount due to an increase in the local topographic slope but this effect is too slight to be seen in *figure 4(a)*.

In *figure 4(b)* we see that as the eddy begins to interact with the seamount, $Y(t)$ increases (that is, 'southward' motion is induced thinking of the β-plane analogy). Because the seamount is 'short' compared to the scale height of the eddy in this simulation, the maximum cross slope deflection is small and corresponds to only about 1.2% of the eddy radius. We can also see that as the eddy passes by the point of maximum height for the
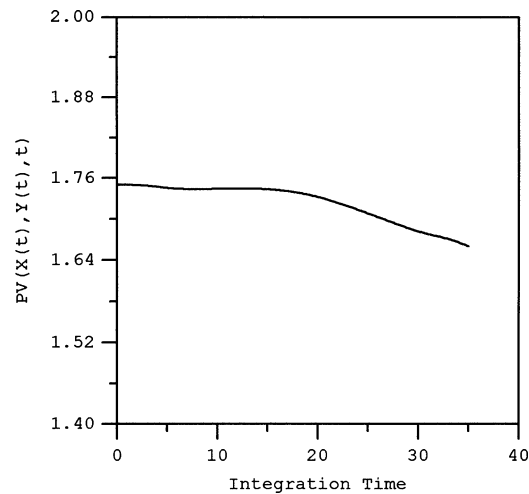
Figure 5. The value of the upper layer potential vorticity, *PV*, following the center mass for the 'short' seamount simulation.

seamount (located at $(0.0, 0.0)$ which occurs at about $t = 18.0$), $Y(t)$ begins to decrease (that is, 'northward' motion thinking of the β-plane analogy). The initial increase and decrease in $Y(t)$ as the eddy directly interacts with the seamount is the result of the topographic steering of the eddy as it the entire flow attempts to conserve the upper layer *PV* following the motion. The decrease in $Y(t)$ continues until after the eddy traverses the seamount and then $Y(t)$ begins to increase again. Longer time simulations (not shown here) show that $Y(t)$ continues to increase linearly and does not oscillate about a reference cross slope position. This later linear increase in $Y(t)$ is the result of the energy which is being radiated away by the topographic Rossby wave tail (Swaters [23]). In *figure 4(c)* we show the path that center of mass follows in the simulation. *Figures 4(c)* and *4(b)* look very much like each other, of course, since $X \approx t$ throughout the simulation.

In *figure 5* we show the value of the upper layer *PV* evaluated following the center of mass versus the integration time for this simulation. Up until the formation of the topographic Rossby wave tail, the *PV* is relatively constant. After the eddy has traversed the seamount there is a decrease in the *PV* following the center of mass. This is a result of the fact that as the wave field radiates energy away $Y(t)$ increases (as shown in *figure 4(b)*) so that $h_B(X, Y) \approx -Y$ (for $\sqrt{X^2 + Y^2} \geqslant 2a$) decreases and thus the upper layer *PV* will decrease.

3.2. Moderate height seamount collision

As the height of the seamount increases the basic qualitative behavior just described remains. However, the quantitative aspects of the interaction are intensified. The cross slope deflection induced by the seamount in larger in amplitude. The topographic Rossby wave tail is larger in amplitude and the cross slope motion induced by the wave tail radiating energy away sets in earlier in the simulation. There is a more intense distortion to the spatial structure of the eddy and the spiral bands are more developed in this simulation and significantly begin to distort the circular shape of the eddy.

In *figure 6* we present gray scale panels of the upper layer stream function or geostrophic pressure $\eta(x, y, t)$ (on the left) and the eddy height $h(x, y, t)$ (on the right) for $t = 8.75$, 17.5 and 35.0, respectively, for the 'moderate height' seamount simulation with $h_0 = 1.0$. The coordinate span and the orientation of each panel is identical to that in *figure 2*. The gray scale is identical to that used in *figure 3*.
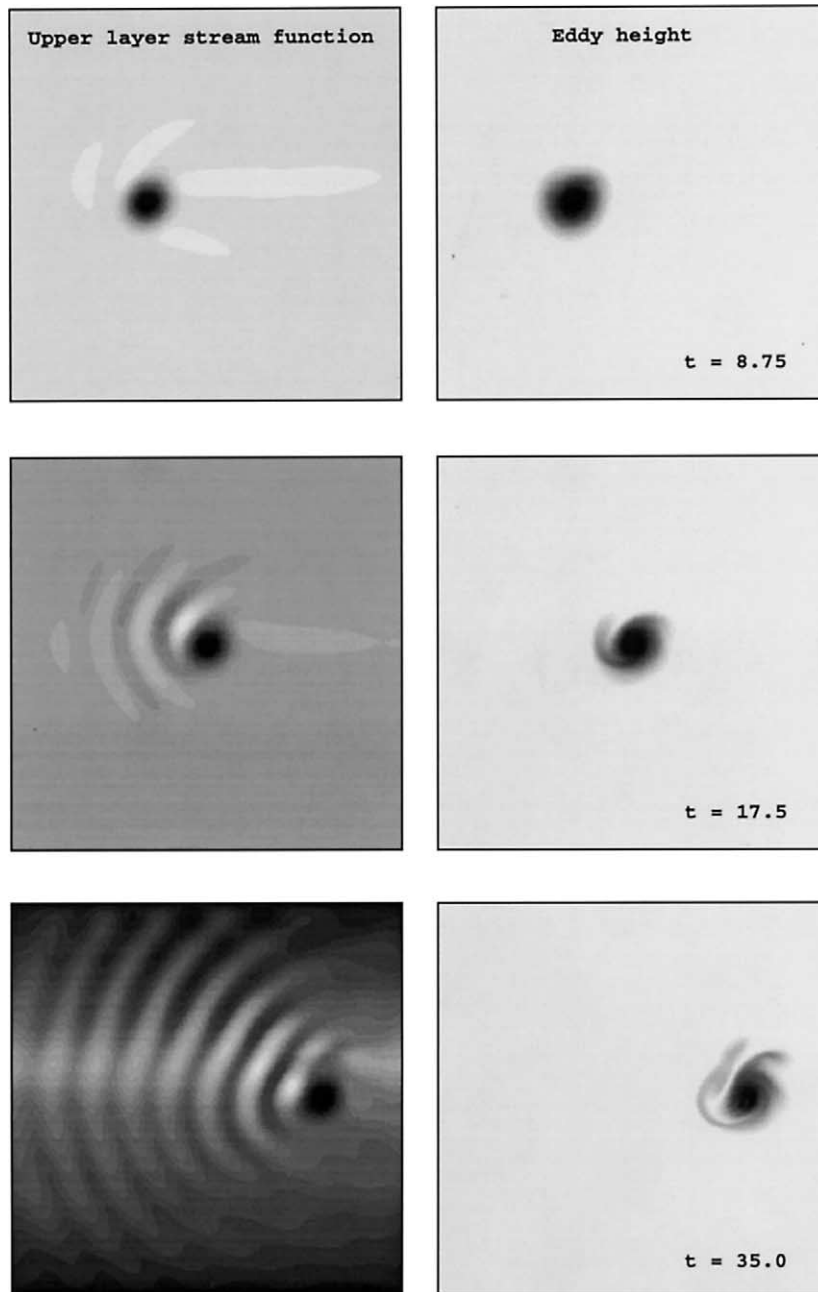
Figure 6. Gray scale panels of the upper layer stream function or geostrophic pressure $\eta(x, y, t)$ (on the left) and the eddy height $h(x, y, t)$ (on the right) for $t = 8.75$, 17.5 and 35.0, respectively, for the 'moderate height' seamount simulation. The coordinate span and the orientation of each panel is identical to that in *figure 2*. The gray scale is identical to that used in *figure 3*.

The $t = 8.75$ panels in *figure 6* correspond to the time at which the eddy is just reaching the edge of the seamount and beginning to collide with it. We can see the initial development of the wave field. Comparing the $t = 17.5$ panels in *figure 6* with those in *figure 3*, we see that the wave field has a larger amplitude at this time in this simulation compared to that shown in *figure 3* as exhibited by the more intense shading in *figure 6*. In

addition, the spiral arms on the eddy boundary are more fully developed in *figure 6* compared to that in *figure 3* at this time. In the $t = 35.0$ panels in *figure 6* one sees that a quite intense wave field has developed in the upper layer and the spiral arms have begun to develop into extended filaments compared to that shown in *figure 3*. Indeed, whereas one could make the argument that the eddy retains its basically radially symmetric structure in the 'short' seamount simulation, this is not the case in the 'moderate height' simulation shown here.

Nevertheless, the along slope speed of the eddy remains relatively close to the Nof speed even in this simulation. In *figure 7* we show the path taken by the center of mass of the eddy, i.e., $(X(t), Y(t))$, for this simulation. Comparing *figure 7* with *figure 4(c)* we see that the along slope distance travelled by the center of mass in this simulation is, to leading order, identical to the 'small' seamount simulation reflecting the fact that along slope speed is well described by the Nof speed here as well.
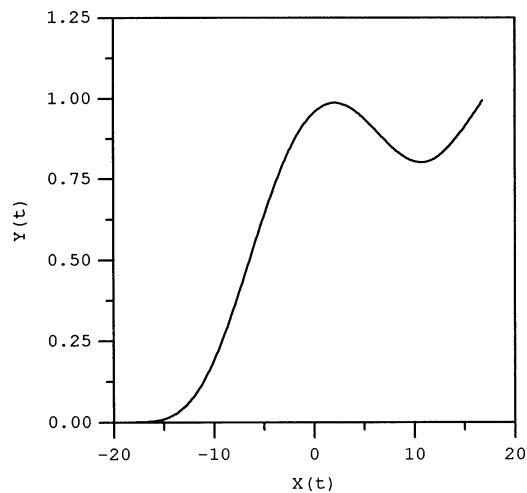

Figure 7. The path taken by the center of mass (X, Y), as determined by numerically evaluating (19) and (20) for the 'moderate height' seamount simulation.
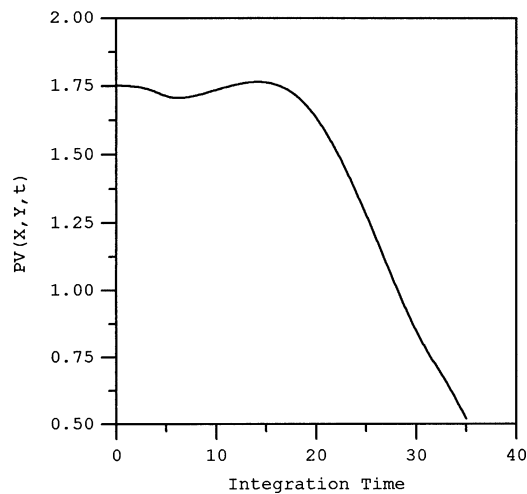

Figure 8. The value of the upper layer potential vorticity, *PV*, following the center mass for the 'moderate height' seamount simulation.

Again, if we compare *figure 7* with *figure 4(c)* we see that the basic pattern of topographically steered cross slope motion induced by the seamount during the initial stages of the collision followed by monotonic cross slope motion induced by the energy being radiated away by the topographic Rossby wave field occurs here as well. However, the wave tail induced down slope motion becomes dominate sooner in this simulation. The eddy does not have a chance to completely traverse the seamount, as it did in the 'short' seamount simulation, before the energy drain associated with the radiating wave field acts to drive the eddy down the sloping bottom toward deep water (or 'southward' thinking of the β-plane analogy). In addition, we see that maximum cross slope deflection which can be associated with the topographic steering is about 10 times larger in amplitude in *figure 7* compared with *figure 4(c)* or about 15% of the radius of the eddy. This scales similarly to the ratio of the seamount heights between the two simulations or, more to the point, to the ratio of the slopes associated with the seamounts in the two simulations.

In *figure 8*, we show the upper layer potential vorticity *PV* following the center of mass $(X(t), Y(t))$ for this simulation. We see that the *PV* remains relatively constant up until $t \simeq 15.0$ after which it monotonically decreases. The slope associated with the decrease in the *PV* is much larger in an absolute sense than that seen in *figure 5* for the 'small' seamount simulation. This reflects the increased down slope velocity associated with the more intense topographic Rossby wave tail in this simulation compared to the 'small' seamount simulation.

3.3. Tall seamount collision

The tall seamount simulation corresponds to a collision between an eddy and a seamount which has a height 5.0 times the scale height of the eddy. Again, while the qualitative properties of this interaction are quite similar to those described for the 'short' and 'moderate height' seamount simulations, the interaction is much more intense.

In *figure 9* we show gray scale panels of the upper layer stream function or geostrophic pressure $\eta(x, y, t)$ (on the left) and the eddy height $h(x, y, t)$ (on the right) for $t = 8.75$, 17.5 and 35.0, respectively, for this simulation. The coordinate span and the orientation of each panel is identical to that in *figure 2*. The gray scale is identical to that used in *figure 3*.

In the $t = 8.75$ panels we can see the development of the topographic wave field in the upper layer as the collision begins. The wave field appears to be slightly more developed in the $t = 8.75$ panel in *figure 9* than in the corresponding panel in *figure 6*. In the eddy height field the spiral arms in *figure 9* are much thicker, that is they are much more developed, than in the corresponding panel in *figure 6*.

Comparing the $t = 17.5$ panels in *figure 9* with those in *figure 6* or *figure 3* we see that the upper layer wave field continues to be substantially more developed in this simulation. Indeed, it almost seems as if the initial monopolar cyclonic structure in the upper layer geostrophic pressure has been overwhelmed by the wave tail and a dipolar structure has emerged with a trailing wave tail. Similarly, the distortion to the eddy boundary is substantially amplified and the spiral arms have already developed into filaments. The circular spatial shape of the initial eddy has been significantly altered by this time in the simulation.

Comparing the $t = 35.0$ panels in *figure 9* with those in *figure 6* or *figure 3* we see that there is essentially no dominant cyclonic eddy in the upper layer by this time in this simulation. The upper layer geostrophic pressure seems to resemble more an arbitrary superposition of topographic Rossby waves than a clearly defined wave tail. The cold dome has elongated into a more or less elliptical shaped vortex structure with filaments. Nevertheless, the eddy, although no longer circular, remains surprisingly coherent and propagates rather steadily.

In *figure 10* we show the path taken by the center of mass of the eddy, i.e., $(X(t), Y(t))$, for this simulation. Here again, if we compare *figure 10* with *figure 7* or *figure 4(c)*, we see that the along slope distance travelled
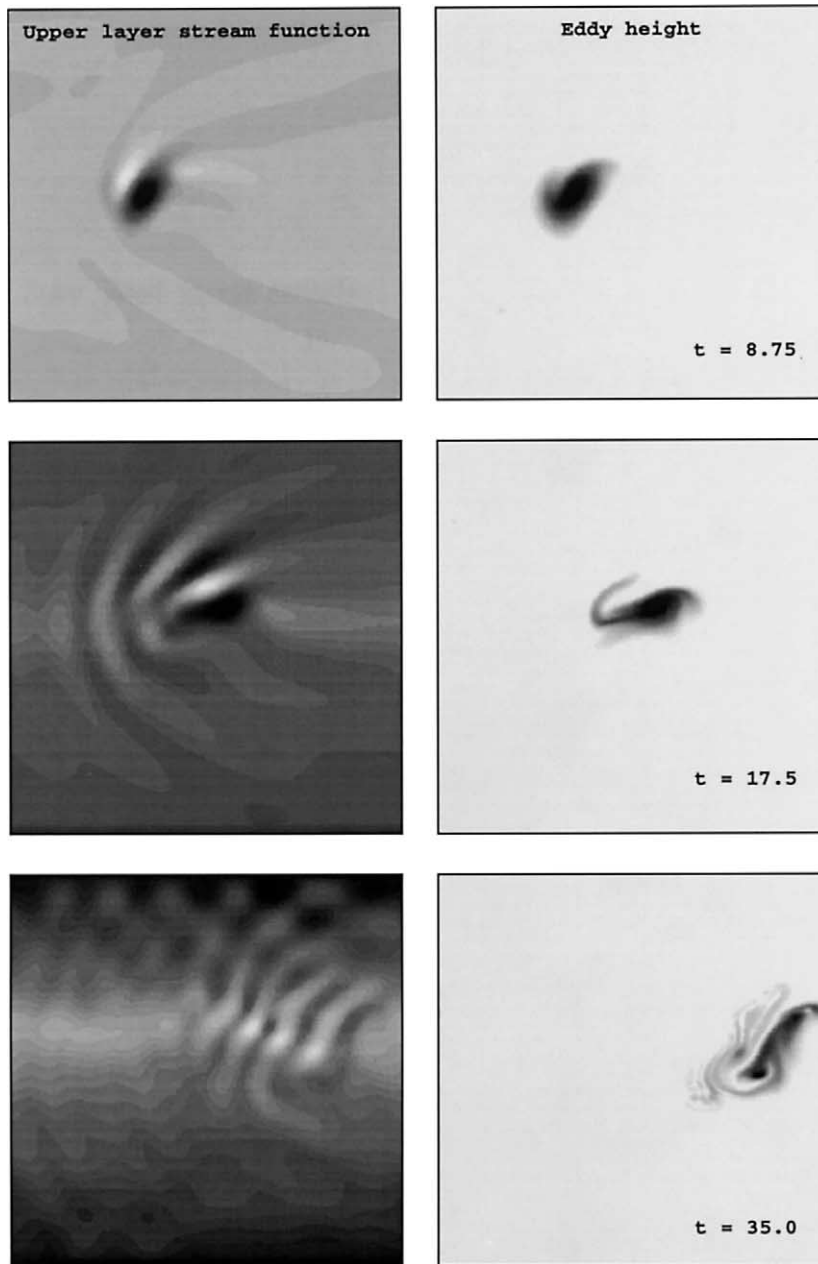
Figure 9. Gray scale panels of the upper layer stream function or geostrophic pressure $\eta(x, y, t)$ (on the left) and the eddy height $h(x, y, t)$ (on the right) for $t = 8.75$, 17.5 and 35.0, respectively, for the 'tall' seamount simulation. The coordinate span and the orientation of each panel is identical to that in *figure 2*. The gray scale is identical to that used in *figure 3*.

by the center of mass is, to leading order, identical in these figures reflecting the fact that the along slope speed is well described by the Nof speed in this simulation. Again, as a result of the larger slopes associated with this 'tall' seamount, the down slope motion of the center of mass due to the effects of topographic steering have a larger cross slope extent. And again, once this stage of the interaction has finished the effects of the upper
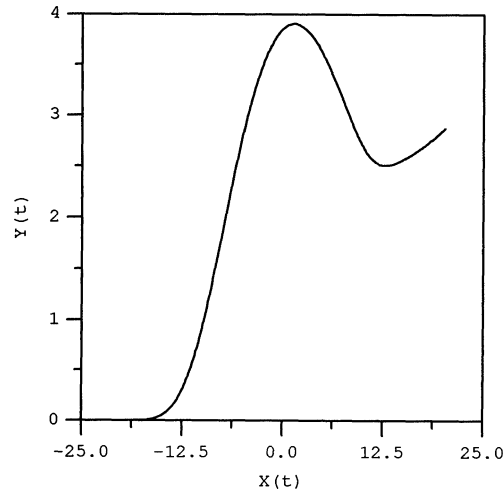
Figure 10. The path taken by the center of mass (X, Y), as determined by numerically evaluating (19) and (20) for the 'tall' seamount simulation.
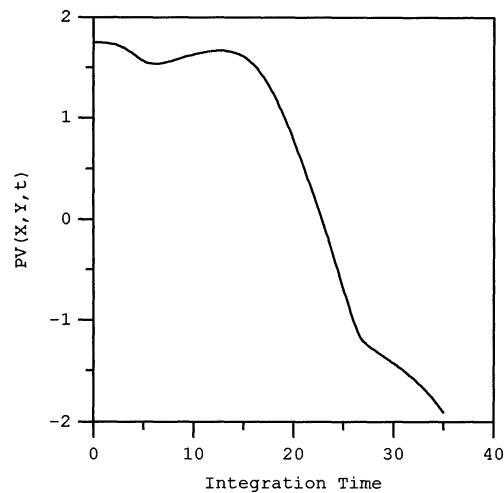

Figure 11. The value of the upper layer potential vorticity, PV, following the center mass for the 'tall' seamount simulation.

layer wave field become dominant and we see the emergence of monotonic down slope motion as the potential energy associated with the cross slope position of the eddy is extracted by the wave field.

However, even with a seamount which is 5.0 times the height the initial eddy the maximum down slope deflection associated with the effects of the topographic steering is only 60% of the eddy radius. Obviously, the maximum down slope deflection is a function both of the slopes associated with the seamount and its diameter. Larger diameter seamounts will generate more substantial cross slope motion.

In *figure 11*, we show the upper layer potential vorticity PV following the center of mass $(X(t), Y(t))$ for this simulation. As in *figure 8*, we see that the PV remains relatively constant up until $t \simeq 15.0$ after which it monotonically decreases. The slope associated with the decrease in the PV is much larger in an absolute sense than that seen in *figure 8* or *figure 5* for the 'small' and 'moderate height' seamount simulations. This reflects the increased down slope velocity associated with the more intense topographic Rossby wave tail in this simulation compared to either of the other simulations.

4. Summary

We have described the collision between deep anticyclonic eddies and seamounts. The model we use to examine the collision between a deep anticyclone or cold dome and a seamount is the two-layer model of Swaters and Flierl [3] and Swaters [4]. This model is based on a sub-inertial approximation to the shallow water equations in which the geostrophic pressure in the upper layer is principally driven by baroclinic vortex-tube stretching and a background topographic vorticity gradient. The lower layer, i.e., the eddy layer, while geostrophic, allows for finite-amplitude thickness variations in order to allow for eddies in the lower layer which possess a genuine incropping in the height field. The mean flow in the lower layer arises primarily due to a geostrophic balance between the Coriolis stress and the down slope gravitational acceleration associated with a relatively dense water mass sitting directly on a sloping bottom. This model filters out barotropic instabilities in the eddy layer and focuses on the baroclinic dynamics of density-driven currents and eddies on a sloping bottom.

In summary, we can describe the collision as follows. As the eddy approaches the seamount and the ambient topographic slope changes, this will lead to changes in the velocity of the center of mass. This effect arises because the eddy propagates as a geostrophically balanced density driven flow on a sloping bottom, that is, it is topographically steered.

On the other hand, as the ambient depth of the upper layer changes due to the presence of the seamount, the other components in the upper layer PV must evolve if it is to be conserved following the motion. As the eddy encounters the seamount it will be deflected to its left or toward positive values of y or, in terms of the β-plane analogy, toward the 'south'.

However, since the seamount does not have a constant slope associated with it individual fluid parcels within the eddy will not necessarily follow a parallel path. Thus, the initial radial symmetry will be lost in the eddy height field leading to a distortion in its shape.

As the eddy begins to spatially distort as it encounters the seamount, Rossby waves will be excited in the upper layer. The topographic Rossby waves act to radiate energy away from the eddy. The source of the energy is the gravitational potential energy associated with cross slope position of the eddy. This down slope, or 'southward' motion, continues even after the eddy traverses the seamount because of the continued action of the wave field. In addition, the dynamical feedback of the topographic Rossby wave on the eddy height field leads to the development of spiral arms on the eddy incropping further distorting the spatial shape of the eddy.

Even with all these dynamical processes occurring two interesting observations remain. First, in all our simulations the along slope motion was well described by the Nof speed. And second, even though the shape of the eddy could get quite distorted, it remained rather coherent and once the principal interaction was over, there didn't seem to be any further rapid development in the shape of the eddy. Thus we have developed a picture which suggests that eddy-seamount interactions may leave these eddies as modified coherent structures which nevertheless can still propagate quite far in the ocean in a more or less quasi-steady manner.

Acknowledgments

References

[1] Swaters G.E., Numerical simulations of the baroclinic dynamics of density-driven coupled fronts and eddies on a sloping bottom, J. Geophys. Res. 103 (1998) 2945–2961.

[2] Richardson P.L., Bower A.S., Zenk W., A census of meddies tracked by floats, Prog. Oceanogr. (2000), in press.

[3] Swaters G.E., Flierl G.R., Dynamics of ventilated coherent cold eddies on a sloping bottom, J. Fluid Mech. 223 (1991) 565–587.

[4] Swaters G.E., On the baroclinic instability of cold-core coupled density fronts on a sloping continental shelf, J. Fluid Mech. 224 (1991) 361–382.

[5] Jiang L., Garwood Jr. R.W., A numerical study of three-dimensional dense bottom plumes on a Southern Ocean continental slope, J. Geophys. Res. 100 (1995) 18471–18488.

[6] Jiang L., Garwood Jr. R.W., Three-dimensional simulations of overflows on continental slopes, J. Phys. Oceanogr. 26 (1996) 1214–1233.

[7] Chapman D.C., Gawarkiewicz G., Offshore transport of dense shelf water in the presence of a submarine canyon, J. Geophys. Res. 100 (1995) 13373–13387.

[8] Gawarkiewicz G., Chapman D.C., A numerical study of dense water formation and transport on a shallow, sloping continental shelf, J. Geophys. Res. 100 (1995) 4489–4507.

[9] Lane-Serff G.F., Baines P.G., Eddy formation by dense flows on slopes in a rotating fluid, J. Fluid Mech. 363 (1998) 229–252.

[10] Choboter P.F., Swaters G.E., On the baroclinic instability of axisymmetric rotating gravity currents with bottom slope, J. Fluid Mech. 408 (2000) 149–177.

[11] Nof D., The translation of isolated cold eddies on a sloping bottom, Deep Sea Res. 30 (1983) 171–182.

[12] Houghton R.W., Schlitz R., Beardsley R.C., Butman B., Chamberlin J.C., The middle Atlantic bight pool: evolution of the temperature structure during 1979, J. Phys. Oceanogr. 12 (1982) 1019–1029.

[13] Pedlosky J., The equations for geostrophic flow in the ocean, J. Phys. Oceanogr. 14 (1984) 448–455.

[14] de Verdiere A.C., On mean flow instabilities within the planetary geostrophic equations, J. Phys. Oceanogr. 16 (1986) 1981–1984.

[15] Poulin F.J., Swaters G.E., Sub-inertial dynamics of density-driven flows in a continuously-stratified fluid on a sloping bottom. I. Model derivation and stability characteristics, P. Roy. Soc. Lond. A 455 (1999) 2281–2304.

[16] Poulin F.J., Swaters G.E., Sub-inertial dynamics of density-driven flows in a continuously-stratified fluid on a sloping bottom. II. Isolated eddies and radiating cold domes, P. Roy. Soc. Lond. A 455 (1999) 2305–2329.

[17] Poulin F.J., Swaters G.E., Sub-inertial dynamics of density-driven flows in a continuously-stratified fluid on a sloping bottom. III. Nonlinear stability theory, Can. Appl. Math. Quart. 7 (1999) 49–69.

[18] Karsten R.H., Swaters G.E., A unified asymptotic derivation of two-layer, frontal geostrophic models including planetary sphericity and variable topography, Phys. Fluids 11 (1999) 2583–2597.

[19] Mory M., Stern M.E., Griffiths R.W., Coherent baroclinic eddies on a sloping bottom, J. Fluid Mech. 183 (1987) 45–62.

[20] Whitehead J.A., Stern M.E., Flierl G.R., Klinger B., Experimental observations of a baroclinic eddy on a sloping bottom, J. Geophys. Res. 95 (1990) 9585–9610.

[21] Mory M., Integral constraints on bottom and surface isolated eddies, J. Phys. Oceanogr. 15 (1985) 1433–1438.

[22] Swaters G.E., Nonlinear stability of intermediate baroclinic flow on a sloping bottom, P. Roy. Soc. Lond. A 442 (1993) 249–272.

[23] Swaters G.E., Dynamics of radiating cold domes on a sloping bottom, J. Fluid Mech. 364 (1998) 221–251.

[24] Arakawa A., Computational design for long term numerical integration of the equations of fluid motion: two-dimensional incompressible flow, J. Comp. Phys. 1 (1966) 119–143.

[25] Asselin R.A., Frequency filter for time integrations, Mon. Weather Rev. 100 (1972) 487–490.

[26] Flierl G.R., Rossby wave radiation from a strongly nonlinear warm eddy, J. Phys. Oceanogr. 14 (1984) 47–58.